

Wasserstein GANs for MR Imaging: from Paired to Unpaired Training

Ke Lei, Morteza Mardani, John M. Pauly, and Shreyas S. Vasawanala

Abstract—Lack of ground-truth MR images (labels) impedes the common supervised training of deep networks for image reconstruction. To cope with this challenge, this paper leverages WGANs for unpaired training of reconstruction networks, where the inputs are the undersampled naively reconstructed images from one dataset, and the outputs are high-quality images from another dataset. The generator network is an unrolled neural network with a cascade of residual blocks and data consistency modules. The discriminator is also a multilayer CNN that plays the role of a critic scoring the quality of reconstructed images. Our extensive experiments with knee MRI datasets demonstrate unpaired WGAN training with minimal supervision is a viable option when there exists insufficient or no fully-sampled training label images that match the input images. Also, supervised paired training with additional WGAN loss achieves better and faster reconstruction compared to wavelet-based compressed sensing.

Index Terms—Wasserstein generative adversarial networks (WGANs), convolutional neural networks (CNN), rapid reconstruction, diagnostic quality.

I. INTRODUCTION

MAGNETIC resonance imaging (MRI) is commonly used clinically for its flexible contrast. The major shortcoming of MRI is its long scan time, especially for volumetric images. Undersampling is often necessary to reduce scan time and cope with motion, but it leads to an ill-posed inverse problem. Reconstructing the true image requires perceptual criteria that capture an expert radiologists perception of acceptable images. Such criteria are complex to model. Learning from training data has been commonly adopted to define perceptual metrics. However, it often requires supervised training with a large and specific set of label images, consisting of fully-sampled high-quality images. We refer to this label image used for training supervision as ‘label’ in this paper.

Collecting such label images is expensive or impossible for scenarios such as dynamic imaging. For instance, in dynamic contrast enhanced (DCE) imaging, the contrast is rapidly changing, or, for deformable moving body organs in the chest, abdomen, or pelvis with respiratory motion, acquiring the ground truth image is a daunting task. On the other hand, basic 2D scans for static body parts, like the body extremities and brain, are often fully-sampled with high enough quality to serve as potential labels. To cope with a small label set or

leverage a large but different label set, semi-supervised (i.e. unpaired) training is the method of choice.

There is ample research during the last few years on deep learning for MRI reconstruction [1]–[9]. However, there are only a few attempts to address the aforementioned challenges such as lack of labels and complex perceptual criteria. Among those, [10]–[14] deploy self-supervision, and [15] deploys transfer learning, so fewer or no labels are needed. In another line of work, the studies in [16]–[20] develop perceptual criteria using generative adversarial networks (GANs), where the entropic GANs (EGANs), or, least-squares GANs (LSGANs) are used. GANs alone, however, do not return satisfactory images. This is due to a GANs drawback, training instability, that causes mode collapse as the learning process overfits the data. This is particularly relevant in the medical imaging domain as the training labels are scarce. To alleviate this issue, most existing studies train on mixture losses with both GANs and pixel-wise losses [16]–[19], [21]. The pixel-wise loss is observed to stabilize the training, discards the high-frequency noise artifacts, and improves the image quality as reported in [16], [18].

Contributions. To develop unpaired training schemes with minimal supervision, we leverage Wasserstein GANs (WGANs) [22]. WGANs improve the training stability of GANs and avoid the mode collapse issues associated with standard GANs. Also, WGANs are more interpretable to evaluate and gauge the quality of reconstructed images. Our WGAN based model consists of a generator (G) and a discriminator (D). The D is a multi-layer plain CNN playing the role of a critic scoring the quality of images denoised by the generator. We extensively examine the performance of different generative models (i.e. plain and unrolled ResNets) under different training scenarios (i.e. paired and unpaired) with different GAN objectives to find the best model given a certain level of labels availability. The unrolled G is a cascade of residual networks (ResNet) [23] and data consistency layers that progressively suppress image artifacts. Experiments with a real-world knee MRI dataset indicate: 1) unpaired WGAN is superior to ℓ_1 -based supervised training, 2) WGAN mixed with ℓ_1 -based training is the best choice when a few paired training samples are available. The main contributions of this paper are summarized as follows:

- Introducing W-GANs to MRI reconstruction for unpaired training with unrolled generator networks
- Optimization of reconstruction via systematic and extensive experiments and comparisons across various GAN objectives for paired and unpaired training

† Work in this paper was supported by the NIH R01EB009690 and NIH R01EB026136 award, and GE Precision Healthcare. The authors are with Stanford University, Departments of Electrical Engineering⁽¹⁾ and Radiology⁽³⁾. Emails: kllei, morteza, pauly, vasawanala@stanford.edu. Part of the results have been submitted to and presented at the 27th annual meeting of International Society of Magnetic Resonance in Medicine (ISMRM), Montreal, Canada, May 2019.

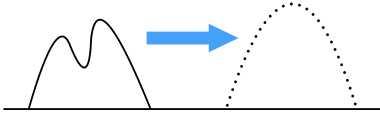


Fig. 1. Illustration of the sand pile transport explanation for earth mover's distance.

The rest of this paper is organized as follows. Section II introduces the preliminaries and states the problem. Paired supervised training and unpaired (semi-supervised) training are discussed in Sections III and IV, respectively. Section V reports the experimental results and evaluations.

Notation. The operators $\mathbb{E}[\cdot]$, $(\cdot)^H$, \odot , $\mathcal{F}\{\cdot\}$, and $\mathcal{F}^{-1}\{\cdot\}$ denote the statistical expectation, matrix Hermitian, Hadamard product, 2D discrete Fourier transform (DFT) and inverse 2D discrete Fourier transform (IDFT), respectively. $\|\cdot\|_1$ and $\|\cdot\|_2$ refer to ℓ_1 and ℓ_2 norm, respectively.

II. PRELIMINARIES AND PROBLEM STATEMENT

MRI reconstruction typically solves a linear inverse system $Y = \Phi y + v$, where Φ captures the forward model of an MRI examination, to find image $y \in \mathbb{C}^n$ from partial frequency domain samples $Y \in \mathbb{C}^m$ ($m < n$) that are contaminated with noise v . Our goal is to learn the inverse neural network map f so that for test data Y we can automatically recover its corresponding y as $f(Y)$. In the supervised/paired approaches, a corresponding label y is given for each input Y during training. In this paper, we consider a practical scenario where a set of noisy observations $\{Y_i\}_{i=1}^M$ is relatively easy to obtain, and the acquisition of a set of high-quality samples (labels) $\{y_j\}_{j=1}^N$ is expensive. That is, in our training dataset, we either have $N \ll M$ or a different set of inexpensive labels, so pairing between y and Y does not exist.

A. Wasserstein distance

Wasserstein distance is a measure of the distance between two probability distributions [24]. One advantage of this metric is that it is continuous everywhere, unlike the Jensen-Shannon (JS) divergence deployed by the original EGANs [25], and χ^2 distance deployed by the LSGANs [26]. We are particularly looking at Wasserstein-1 distance in this paper. It is also known as the earth-mover's (EM) distance (also see Fig. 1). This quantity intuitively reflects the minimum cost (i.e., mass times distance) to transport a pile of sand to another pile (with different location and shape). Formally, the Wasserstein-1 distance between probability mass P_r and P_g is defined as

$$W(P_r, P_g) = \inf_{J \in \mathcal{J}(P_r, P_g)} \int \|x - y\|_1 dJ(x, y) \quad (1)$$

where $\mathcal{J}(P_r, P_g)$ is the set of all joint distributions for x and y whose marginals are P_r and P_g , respectively.

B. From Wasserstein distance to Wasserstein GAN

The objective of GANs is to mimic a desired 'real' distribution (P_r) by minimizing the distance between the 'fake'

distribution (P_g) of G outputs and that of the labels. WGAN is minimizing the Wasserstein-1 (1) distance specifically. The infimum in (1) is highly intractable, but using Kantorovich-Rubinstein duality one can alternatively write it as

$$W(P_r, P_g) = \sup_{\|f\|_L \leq 1} \mathbb{E}_{x \sim P_r}[f(x)] - \mathbb{E}_{x \sim P_g}[f(x)] \quad (2)$$

where the supremum is over all the 1-Lipschitz functions f . We use a D network to define a smooth f which aims to separate the real and fake distributions as far as possible while G aims for the opposite. In this way, D serves as a critic which scores the quality of the G output. Formally, the training objective for WGAN is

$$\min_G \max_{\|D\|_L \leq 1} \mathbb{E}_{y \sim P_r}[D(y)] - \mathbb{E}_{x \sim P_g}[D(x)] \quad (3)$$

where the maximum is over all the 1-Lipschitz discriminators D . x and y refer to the G output and label, respectively.

In practice, it is hard to satisfy the Lipschitz continuity constraint in (3), thus [27] introduces a viable alternative using gradient-norm regularization. In principle, according to [27, Proposition 1], the optimal critic must have the end-to-end gradient equal to unity for the convex combinations of samples drawn from real and fake distributions. This indicates that for any random sample $\hat{x} := \alpha x + (1 - \alpha)y$ with y and x from real and fake distributions, respectively, and $0 \leq \alpha \leq 1$, one can use the gradient penalty as

$$\min_G \max_D \mathbb{E}_{y \sim P_r}[D(y)] - \mathbb{E}_{x \sim P_g}[D(x)] + \eta \mathbb{E}_{\hat{x} \sim P_{\hat{x}}} (\|\nabla_{\hat{x}} D(\hat{x})\|_2 - 1)^2.$$

III. GAN TRAINING FOR IMAGING

Supervised learning of the inverse mapping is common in the MR imaging context using pixel-wise losses. They achieve stable training but the resulting images are typically blurry especially at high undersampling rates. To gain insights about this phenomenon, consider the intersection of all feasible images for the linear measurements $Y = \Phi y$. Let us denote this affine subspace by $\mathcal{C} \subset \mathbb{C}^n$. Denote the manifold of real images also by \mathcal{S} . The unknown image of interest lies in the intersection $\mathcal{C} \cap \mathcal{S}$. From a probabilistic point of view, the intersection may have several images with different prior values. The supervised pixel-wise training based on ℓ_2 -loss essentially returns the mean image in the intersection. Likewise, ℓ_1 -minimization returns the median image. The GAN training advocated in [18] however can achieve the most plausible image that coincides with the maximum a posteriori (MAP) estimate [28].

The GAN training alone suffers from high-frequency artifacts, especially when using EGANs and LSGANs. This mainly emanates from the unstable training of GANs with stochastic gradient descent. In essence, EGANs and LSGANs are based on JS and χ^2 divergences that tend to infinity for disjoint real and fake distributions. As a result, the gradients are not informative for training. WGAN, however, offers stable training owing to the continuity of the Wasserstein-1 distance (w.r.t. network parameters). It thus provides informative gradients even when the real and fake distributions are far apart; see e.g., [22] for concrete examples.

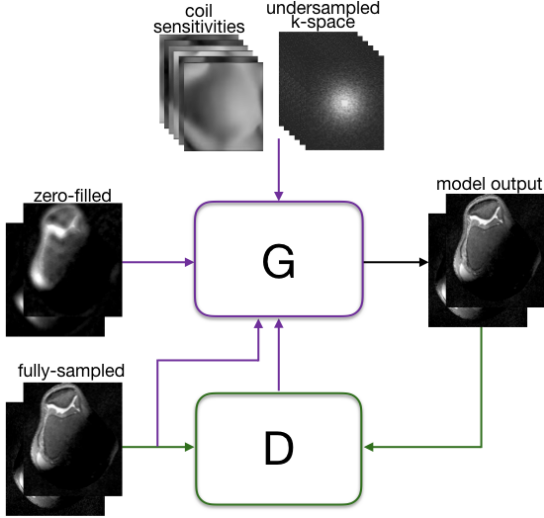


Fig. 2. Paired GAN training with pixel-wise supervision.

In addition to GANs loss, we use pixel-wise supervision with the available high-quality labels. We will deal with completely unpaired training in the next section. In the training process, the input to G is a simple linear reconstruction from the zero-filled (ZF) k-space measurements and coil sensitivities extracted by the ESPIRiT algorithm [29]. D then assigns a score to each of its input, which is as low as possible on generated data, and as high as possible on real data. G aims to output images close to the ground-truth label in terms of ℓ_1 distance, and simultaneously gain a high score from D. The training objectives for G and D are given as follows

$$(P1.D) \quad \min_{\Theta_d} \mathbb{E}[D(x; \Theta_d)] - \mathbb{E}[D(y; \Theta_d)] \\ + \eta \mathbb{E}[(\|\nabla_{\hat{x}} D(\hat{x}; \Theta_d)\|_2 - 1)^2]$$

$$(P1.G) \quad \min_{\Theta_g} -(1 - \lambda) \mathbb{E}[D(G(x_{zf}; \Theta_g); \Theta_d)] \\ + \lambda \mathbb{E}[\|y - G(x_{zf}; \Theta_g)\|_1]$$

where $x_{zf} = \Phi^H Y$ is the ZF image (G input), and $x = G(x_{zf}; \Theta_g)$. Θ_g, Θ_d denote parameters for G and D respectively, and they are updated in an alternating fashion based on stochastic gradient descent. The last term in (P1.D) is the gradient penalty (GP) with η parameter that enforces 1-Lipschitz constraint for D. Figure 2 illustrates the paired training procedure of our model.

SGD algorithm. The optimization for (P1.D) and (P1.G) is performed during training for each mini-batch size b . First, the random samples $\{\hat{x}_i\}_{i=1}^b$ are drawn by uniformly sampling b different α s as discussed in Section II.B. The mini-batch gradient of (P1.D) w.r.t. Θ_d is calculated given the labels $\{y\}_{i=1}^b$, the G outputs $\{x_i\}_{i=1}^b$, and random samples. Likewise, the G gradient (P1.G) is calculated, and the gradient steps are updated iteratively.

A. Unrolled generator networks

The G network takes the zero-filled input image, x_{zf} , which masks the k-space with $\Omega \in \{0, 1\}^n$. The zero-filled image is

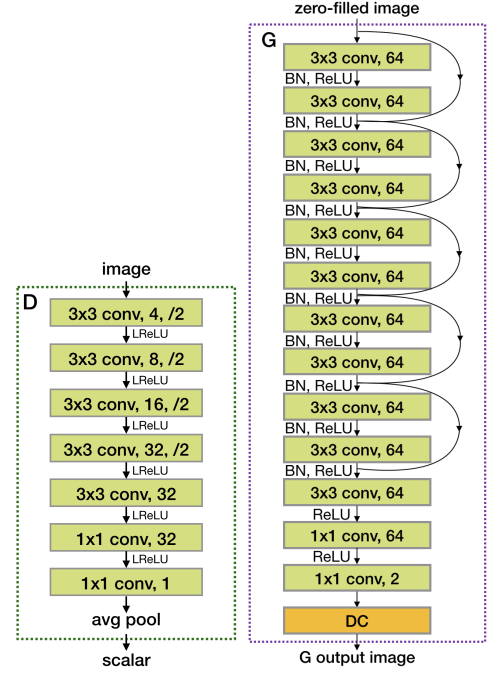


Fig. 3. The discriminator network (left) and plain generator network with hard DC (right). BN and ReLU are applied after the summation with skip connections.

simply an IDFT on the masked k-space and is of very low quality. Since both k-space and image are complex-valued, two channels are used to represent real and imaginary parts. G is designed to suppress the aliasing artifacts from the zero-filled input image.

We start with a standard ResNet [23] for G, as shown in Fig. 3. This is the same network as that in [18]. The plain network entails many training parameters that increase the training overhead and more importantly limit their generalization performance for medical imaging tasks where high-quality labels are scarce.

Recently, unrolled networks were introduced, which show superior performance for image recovery and restoration tasks [7], [30]–[32]. They are inspired by iterative inference algorithms [33]. In particular, the unrolled network implements iterations of proximal gradient descent algorithm given by

$$x_{k+1} = \text{Prox}(x_k + \mu \Phi^H (Y - \Phi x_k)) \quad (4)$$

where Prox is a proximal operator that encourages some prior distribution (e.g., sparsity) for the images, and μ is a small step size. In order to learn the proximal from data, we model them with NNs (ResNet). The iterative process can be envisioned as a state-space model which at the k -th iteration takes an image estimate x_k , moves it towards the affine subspace of data consistent images, and then applies a proximal operator to obtain x_{k+1} . The state-space model is expressed as

$$v_{k+1} = g(x_k) \quad (5)$$

$$x_{k+1} = NN(v_{k+1}) \quad (6)$$

where g is data consistency (DC) with a learnable step size μ that combines the ZF data with output of the previous

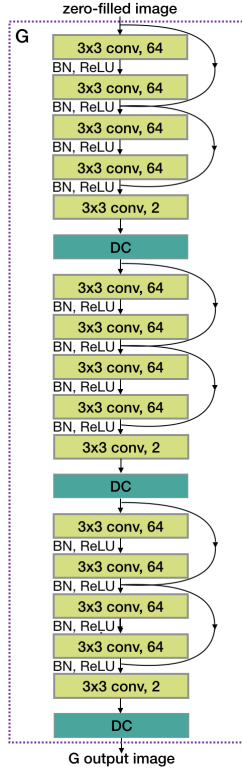


Fig. 4. The unrolled generator network with soft DC.

iteration, x_k . Unfolding this recursion for a fixed number K of iterations, one ends up with a recurrent NN (Fig. 4), where x_K is the generator output.

The data consistency (DC) step ensures the k-space of the generated image is consistent with the actual input k-space data. One can imagine hard and soft DC. Soft DC is a gradient descent step

$$g(x) = x + \mu \left[\sum_{i=1}^c \mathcal{F}^{-1} \{ \Omega \odot \mathcal{F} \{ x \odot s_i \} \} \odot s_i^H - x_{zf} \right] \quad (7)$$

where there are c coil maps $s_i \in \mathbb{C}^n$. Alternatively, one can apply a hard DC with no need for learnable parameters as

$$g(x) = \sum_{i=1}^c \mathcal{F}^{-1} \{ Y_{\Omega}^i + (1 - \Omega) \odot \mathcal{F} \{ x \odot s_i \} \} \odot s_i^H \quad (8)$$

where $Y_{\Omega}^i \in \mathbb{C}^n$ is the zero-padded k-space measurement from the i th coil.

B. Discriminator network

D has two inputs from the G output and the real samples, both are complex-valued that require two channels. D also outputs a real-valued scalar and involves no soft-max. A 7-layer plain CNN is used for D as shown in Fig. 3, where the architectural details are provided in the figure. For the first four layers, the number of feature maps is doubled from 4 to 32, and a stride of 2 is used. Leaky ReLU nonlinearity (LReLU) [34] activation is used for all layers except the last one. The last layer averages out the seventh layer features to end up with a scalar score.

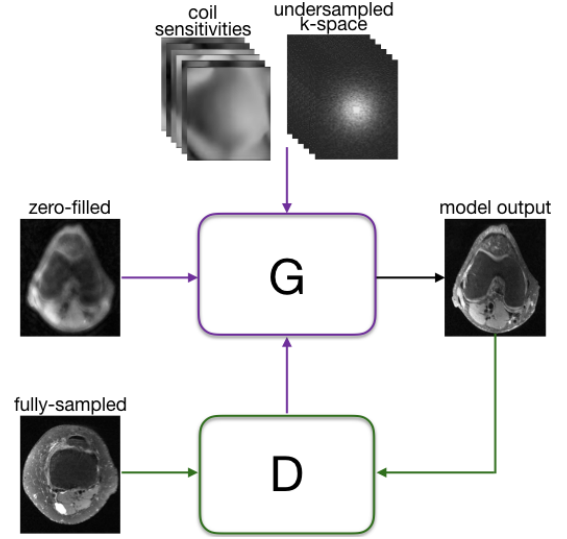


Fig. 5. Unpaired GAN training.

IV. UNPAIRED GAN TRAINING

The ground-truth label is often not present for certain imaging scenarios that serve as input to our advocated GAN based reconstruction scheme. It is thus important to relax the pixel-wise supervision completely so that no pairing is needed. Then, one can leverage the available labels from other datasets that are more amenable to fully sampled acquisition. For instance, using 2D images as training labels and cine imaging frames as inputs.

In principle, training of GANs is derived to minimize a distance between the underlying ground-truth data distribution and the distribution implicitly defined by the outputs of the G. Since we are only working with distributions, only the dataset as a whole matter, and no pairing is needed. The G is responsible for inverting the partial Fourier undersampling to mimic the distribution of real images. D aims to score the G output quality, which should be as low as possible for generated data, and as high as possible for real data. Unpaired training has proved successful in image style transfer tasks (for instance, converting zebras to horses, and vice versa) such as [35] with pure GAN training. These tasks in natural images do not necessarily require authentic output images.

Pure GAN training for medical images, however, introduces a hallucination risk. The pixel authenticity is crucial and needs to be guaranteed. GANs are subject to overfitting (related to mode collapse) [36] especially for medical image datasets that are typically small. Fortunately, for the considered de-aliasing problem one has the k-space data and the forward model at hand to somewhat enforce the G outputs to adhere to the k-space data. Indeed, this is ensured by the DC layers embedded into the unrolled generator architecture in Section III.A. DC however partially alleviates the hallucination risk, but overfitting is still a risk.

Pure GAN training based on the classic GANs such as EGANs and LSGANs is tricky to train stably, and suffers from mode collapse. During the training process, G only receives scalar-valued (global) feedback from D and does not see the

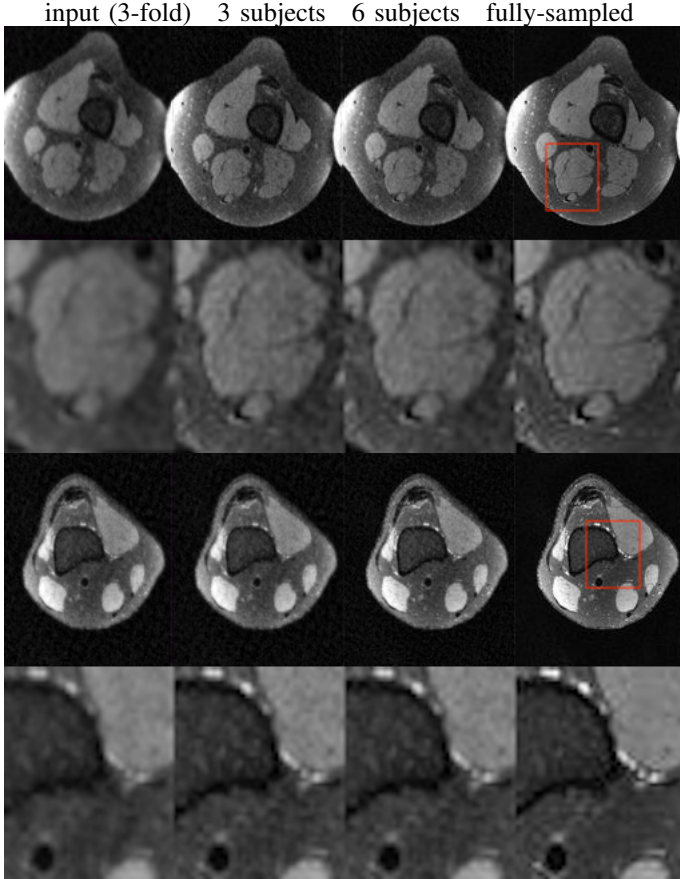


Fig. 6. Two representative test samples from the single-coil model. From left to right: 3-fold undersampled input, output from our model trained with 3 subject and 6 subject labels, and fully-sampled reference.

image details to preserve the pixel-level contents. This can lead the game between G and D to trap into a sub-optimum equilibrium. In essence, GAN training is unstable mainly due to the uncertainty from the alternating gradient updates. For instance, if D becomes stronger than G at some point, it would distinguish all fake inputs, and as a result, G receives no informative feedback (always negative) to generate better images.

In our experiments, we observe that unsupervised GAN training based on EGANs and LSGANs leads to corrupted (i.e. with coherent artifacts) images in both the test and train phases; see section V.B. for details. This motivates using WGANs [27] for MRI. As discussed before, WGAN offers more stable training than other GANs since the distribution distance, namely Wasserstein-1 distance, is continuous everywhere. However, the distances used by classic GANs, namely JS divergence for EGANs [25], or χ^2 divergence for LSGAN [26], becomes infinity when the distributions tend to be loosely overlapping. This commonly happens when training with image distributions that are in high-dimensional spaces.

The plain D network in the unpaired case can take single-channel magnitude images – an option in addition to taking two-channel complex-valued images as in the paired case. We explore this relaxation so that datasets which only consist of magnitude images and no k-space data can also be used as

labels. The G network is the same as in the paired training case. The training objective for the D is the same as in (P1.D), where the training objective for G is derived upon choosing $\lambda = 0$ in (P1.G).

V. EXPERIMENTS

The effectiveness of the unpaired WGAN scheme is assessed for single- and multi-coil MR acquisition model with Cartesian sampling. Extensive experiments are performed to examine whether unpaired WGAN can lead to faithful reconstructions, and compare paired WGAN with other paired approaches using EGANs, LSGANs, or only pixel-wise loss (i.e. ℓ_1 -net).

Knee MRI dataset. This dataset includes 19 subjects scanned with a 3T GE MR750 whole-body MR scanner at the Stanford Lucile Packard Children’s Hospital [37]. Fully sampled images are acquired with a 3D FSE CUBE sequence with proton density weighting including fat saturation. Other parameters include FOV = 160mm, TR = 1550 (sagittal) and 2,000 (axial), TE = 25 (sagittal) and 35 (axial), slice thickness 0.6mm (sagittal) and 2.5mm (axial). For each subject we have a complex-valued 3D volume of size $320 \times 320 \times 256$. Axial slices of size 320×256 are the input for training and test. For the unbalanced case, 17 subjects are used for training and 2 subjects for testing. For the disjoint case, 13 subjects are used for training and 6 subjects for testing.

A. Network architecture and training

The plain G network is a deep ResNet [23] with 5 residual blocks (RBs) followed by 3 Conv layers. The D network consists of 7 Conv layers with LReLU nonlinearity; see Fig. 3. Also, as shown in Fig. 4, the unrolled G has 3 iterations, each with two RBs. Batch normalization (BN) [38] and ReLU are used after each layer except the last Conv layer for both plain and unrolled G. We set the gradient penalty coefficient $\eta = 10$. Adam optimizer is used with the momentum parameter $\beta = 0.9$, mini-batch size 4, and learning rate 10^{-4} . For paired GAN+ ℓ_1 training, $\lambda = 0.99$ is used. Fully-sampled images are windowed to increase the brightness of the labels. The model is implemented in Tensorflow and the source code is available online at GitHub¹.

B. Unpaired training of WGAN versus LSGAN and EGAN

We start with a single-coil scenario and show that WGAN is superior to LSGAN and EGAN. Here only the plain G network is used. Undersampled data are obtained by applying a n -fold undersampling mask to the ‘k-space’ of the fully-sampled image. Fully-sampled k-space in the single-coil case is obtained by a 2D DFT of the complex-valued fully-sampled image. The model is trained using fully-sampled volumes from 3 and 6 subjects, and undersampled volumes from 17 subjects.

We tried recovering inputs undersampled by 3-, 4- and 5-fold masks. GANCS trained without ℓ_1 loss, that is, with merely LSGAN loss, or, EGAN loss, cannot output usable result for 3-fold undersampled input (see Fig. 7). A sample

¹<https://github.com/lisakelei/Unpaired-GANCS/>

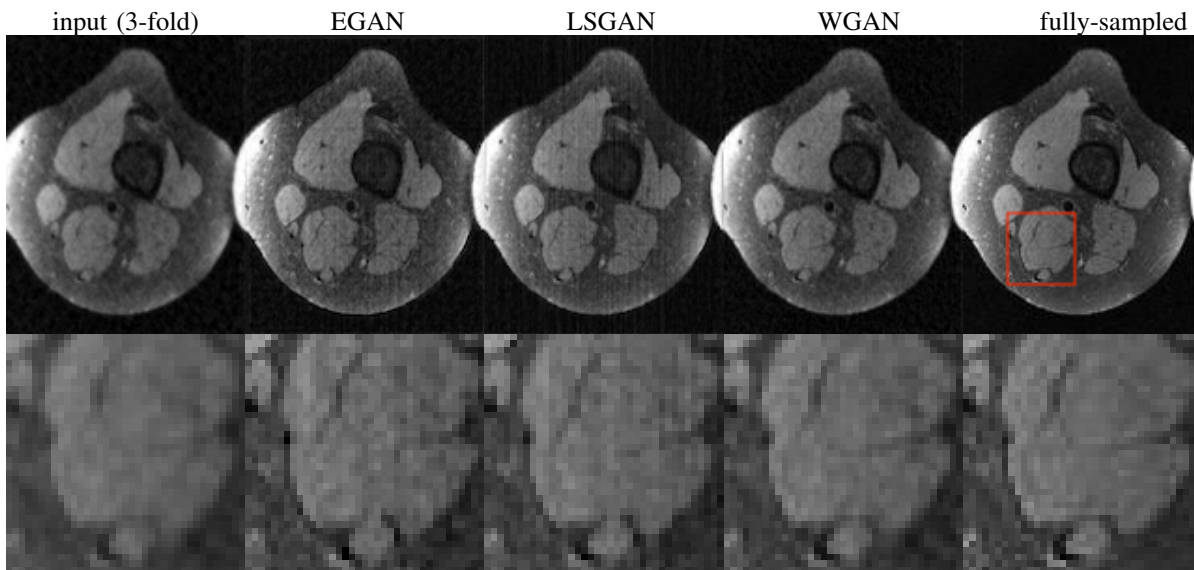


Fig. 7. A representative test sample from the single-coil plain G model trained with 6 subject labels and various unpaired GAN objectives: EGAN, LSGAN, WGAN-GP. The bottom row shows the region in red box zoomed-in.

image from WGAN with a different number of training images is depicted in Fig. 6. The reconstructed images from 3-fold undersampling are diagnostically valuable even when using a small (only 3) number of label subjects. Increasing the undersampling rate to 4-fold the images are acceptable. For 5-fold the images are too noisy to provide accurate details.

C. Robustness against training labels

All experiments beyond this point are done for a multi-coil forward model with k-space data from 8 coils. We perform unpaired training under different scenarios of label availability. *Unbalanced sets of input and label.* We tested the plain G network under various numbers of labels. Undersampled image volumes from 17 subjects are used as the input, and only 3 or 6 of the fully-sampled volumes as labels. We tried various undersampling ratios (5,7,9). Quality of the output images varies with the undersampling ratio (i.e. quality of the input), but outputs from a model trained with 3 subjects are not significantly worse than that from the model trained with 6 subjects. All outputs look reasonable but blurrier compared to those from the unrolled G. Table I lists the average SNR and SSIM over slices in two test volumes.

Disjoint sets of input and label With the better performing unrolled G network, we explore a more relaxed setting for the labels where there is no overlap between the input and label sets, i.e. undersampled raw data from 7 subjects as inputs, and fully-sampled images from other 6 subjects as labels. This setting is useful when we want to train a model for a dataset with any label using high-quality labels from some other datasets. Experiments in this disjoint setting are discussed in the next subsection.

D. Different configurations and losses for unpaired WGAN

We first show that when using the plain G networks, even unbalanced WGAN training with partial labels gives

perceptually better results than paired ℓ_1 training (with full labels). We then switch to the unrolled G and compare models trained with various unpaired objectives.

Plain G. Compared to a model trained with pixel-wise losses (i.e. ℓ_1 , ℓ_2), our model trained with pure WGAN loss not only allows for using fewer labels but also generates images with more realistic texture. Pixel-wise paired training (with double the labels of the unpaired training) while refining the edges better, oversmooths images. Fig. 8 shows the outputs from unpaired WGAN loss compared with that from paired ℓ_1 training. Table I lists the average SSIM [39] and SNR of output test images from the plain G trained under different unpaired settings for various undersampling rates.

Unrolled G. With 3 iterations of unrolled G, we get more accurate images (with around 2dB better SNR) compared to plain G. We examine the model under *disjoint* sets of input and labels. Unpaired training is performed with the following three objectives and results are compared with conventional compressed sensing (CS).

We trained the model with pure WGAN-GP objective on 8-fold and 10-fold variable density masked inputs. A sample comparison between the 8- and 10-fold experiments is shown in Fig. 9. The inference sample and quantitative score from this model along with some other models are shown in Fig.11 and Table II. The quantitative scores are averaged over 1920 test slices, and only the center 272 x 216 region out of a 320 x 256 image is used.

Inspired by the regularizations commonly used in CS, we add total variance (TV) and wavelet loss, calculated based only on the generator output, to the WGAN loss for training. We tried a weighting factor of 1, 10 and 100 for both TV and Wavelet loss (factor of 1 for WGAN) for training on 10-fold variable density Poisson masked input. All gave similar results that are worse than using WGAN loss alone. We observe that even with pure WGAN training, the TV and Wavelet

TABLE I
 QUANTITATIVE EVALUATIONS OF THE MULTI-COIL PLAIN MODEL WITH UNPAIRED WGAN OR PAIRED ℓ_1 LOSS, WITH 5 TO 9-FOLD UNDERSAMPLED INPUTS, AND 3 TO 17 SUBJECT LABELS FOR TRAINING.

| Experiments | ℓ_1 5-fold 17 subj | 5-fold 6 subj | 5-fold 3 subj | 7-fold 6 subj | 7-fold 3 subj | 9-fold 6 subj | 9-fold 3 subj |
|-------------|-------------------------|---------------|---------------|---------------|---------------|---------------|---------------|
| SNR | 18.76 | 18.81 | 18.48 | 17.66 | 17.23 | 16.72 | 16.34 |
| SSIM | 0.591 | 0.873 | 0.869 | 0.842 | 0.835 | 0.819 | 0.813 |

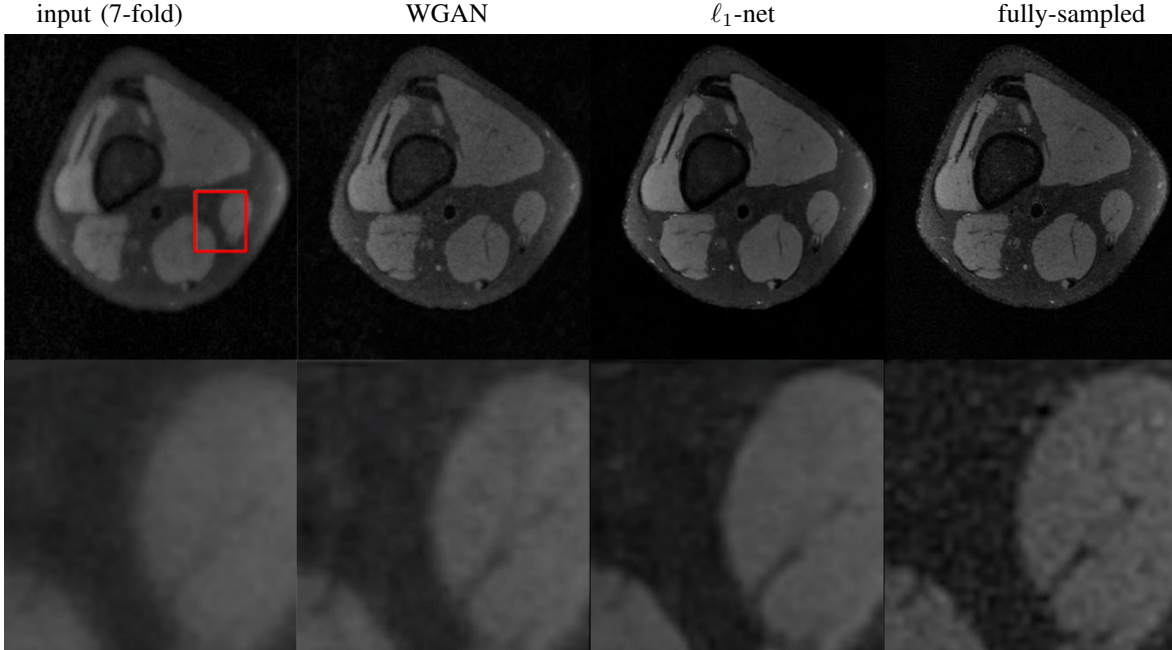


Fig. 8. A representative test sample from the multi-coil plain model trained with various objectives. From left to right: 7-fold undersampled input, output from our unpaired model trained with 6 subject labels, output from the same G trained with pure ℓ_1 loss and 17 subject labels, fully-sampled reference.

loss of the train time generator output decreases to a level that's close to that trained with TV and Wavelet objective. This might be one reason why adding the two losses does not help. An inference (i.e. test) sample from these two models with a weighting factor of 10 for non-GAN loss compared with the pure WGAN model is shown in Fig. 10.

CS-Wavelet. CS reconstruction images by the BART [40] toolbox are considered. The regularization parameters 0.05 is tuned to optimize for the perceptual quality of a small evaluation set. Sample reconstructed slices are shown in Fig. 11 and Fig. 12.

Overall, the comparisons among these schemes and configurations indicate unrolled ResNets with WGAN training as the viable alternative to CS.

E. Paired training

In this section, we consider a supervised scenario with input and label pairs from 6 subjects. Inputs are undersampled by 10 fold. The network is again trained with unrolled G and two different objectives.

We first train WGAN+ ℓ_1 net. During training, the first 500 batches with pure ℓ_1 loss, then linearly decrease the ℓ_1 loss weighting factor to 0.99, and increase the WGAN loss to 0.01 within the first 1000 mini-batches. This is useful to stabilize training and improve final performance. We then, train the

model with only ℓ_1 loss, which we find is always better than ℓ_2 loss. The results are not as sharp as that from the same model trained with additional WGAN loss. Two test slices from these two models are shown in Fig.11 and 12, and the quantitative scores are shown in Table II. The bottom line is that when paired training is possible, adding WGAN objective to the classic ℓ_1 -minimization leads to results that are visually sharper with higher SNR.

F. Radiologist evaluation

To quantitatively assess the image qualities from different reconstruction methods, we performed an experiment based on the expert opinion of two radiologists. We asked each radiologist to rank the reconstructed volumes given by four reconstruction methods together with the fully-sampled volume according to five aspects: sharpness, level of coherent artifacts, visibility of anterior cruciate ligament (ACL), medial meniscus (MM) and medial collateral ligament (MCL). ACL, MM, and MCL are three structures in the knee that are mostly inspected.

Image volumes from 6 different subjects are used. The radiologists are then presented with 30 image volumes. Radiologists are blind to the reconstruction schemes thus treat all 30 volumes equally. Horos [41] software interface is used to visualize the images. The ranking is decided upon discussion

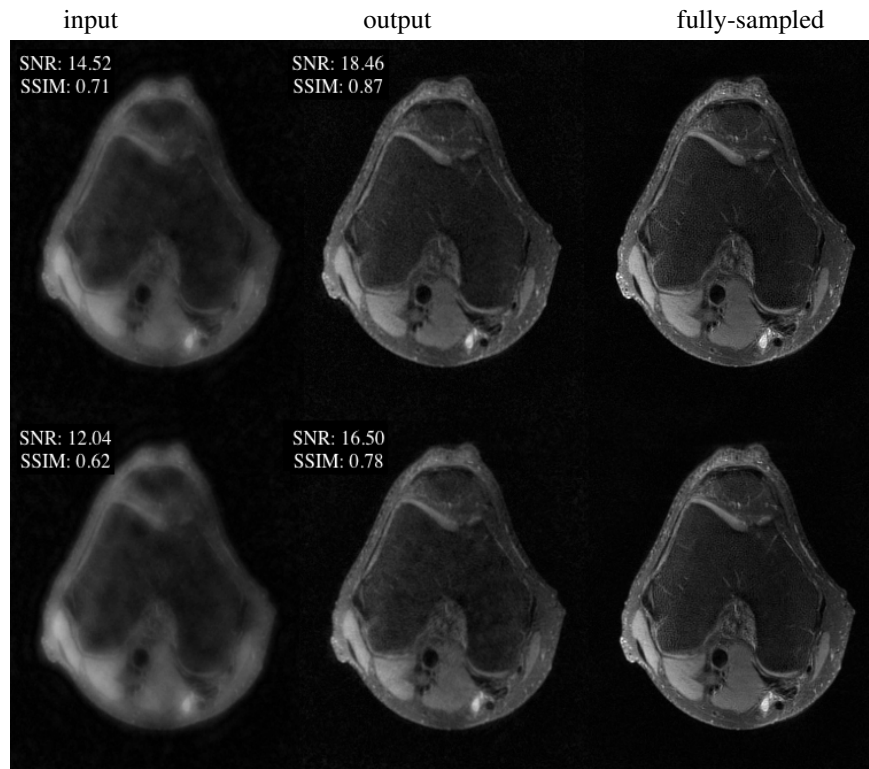


Fig. 9. A representative test sample from the unpaired multi-coil unrolled model with various inputs. From left to right: n -fold undersampled input, corresponding output from our model trained with 6 subject labels, fully-sampled reference. From top to bottom: experiments with 8, 10-fold undersampled inputs.

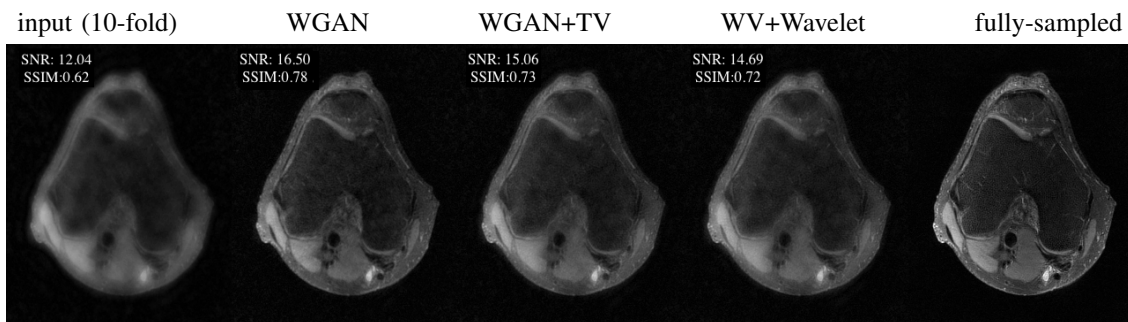


Fig. 10. A representative test sample from the unpaired multi-coil unrolled model trained with various objectives and 6 subject labels. From left to right: 10-fold undersampled input, outputs from model trained with WGAN, WGAN+TV, WGAN+Wavelet losses, fully-sampled reference.

TABLE II
QUANTITATIVE EVALUATIONS OF THE MULTI-COIL UNROLLED MODEL TRAINED WITH DIFFERENT OBJECTIVES COMPARED WITH CS-WV.

| | input (10-fold) | WGAN | ℓ_1 | WGAN+ ℓ_1 | CS-Wavelet |
|------|-----------------|-------|----------|----------------|------------|
| SNR | 12.57 | 16.52 | 16.84 | 17.05 | 16.96 |
| SSIM | 0.69 | 0.82 | 0.83 | 0.82 | 0.85 |

and consensus between two radiologists. For each subject, the five volumes (for different reconstructions) are ranked from best to worst with ties possible. We then convert the rankings to scores; the best score is 5, and the worst one is 1. When there is a tie, we take an average of the scores; for example, if second and third best scores are equally good, both would receive the score $\frac{4+3}{2} = 3.5$. The scores are presented in Fig. 13.

G. Inference time

Table III shows the inference time for reconstructing each 2D slice in a NVIDIA TITAN Xp GPU [42]. The listed time excludes reading and writing, and is averaged across two test volumes. The 3-iteration unrolled network is only slightly slower than the plain network, while both NN based models are significantly (16 times) faster than the conventional CS-Wavelet.

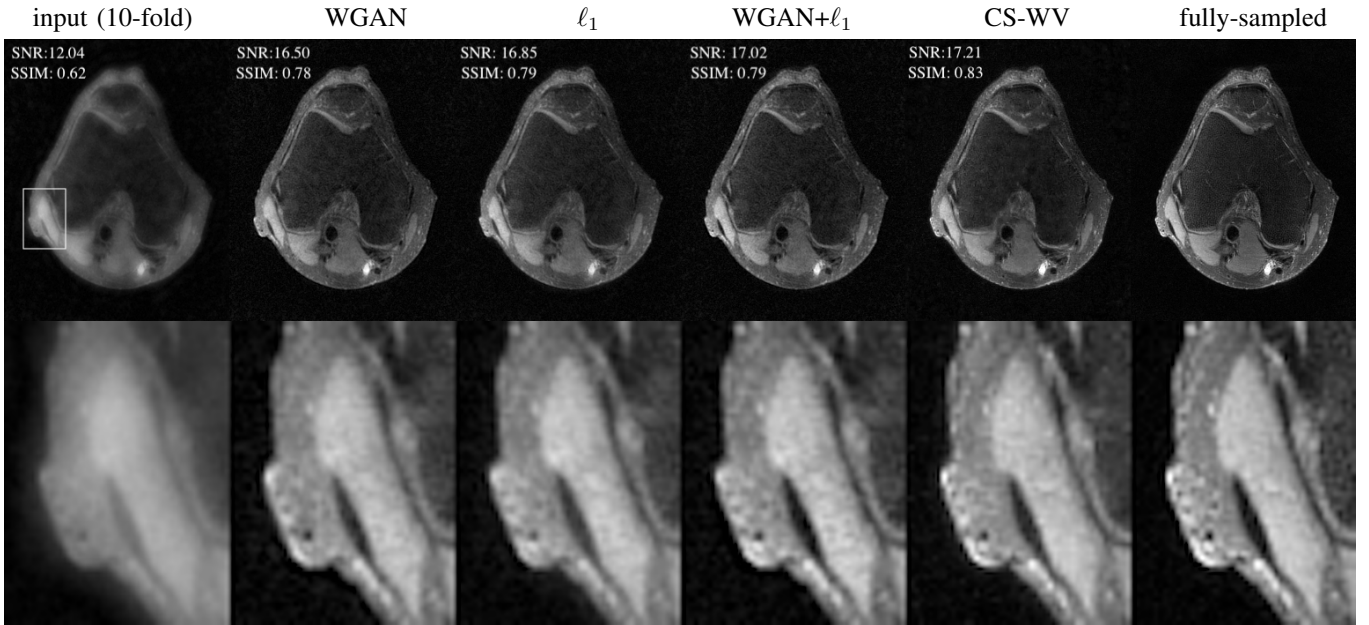


Fig. 11. Test samples from the multi-coil unrolled model trained with various objectives compared with CS. From left to right: 10-fold input, outputs from unpaired model trained with WGAN, paired model trained with ℓ_1 , paired model trained with WGAN and ℓ_1 , CS-Wavelet, fully-sampled reference.

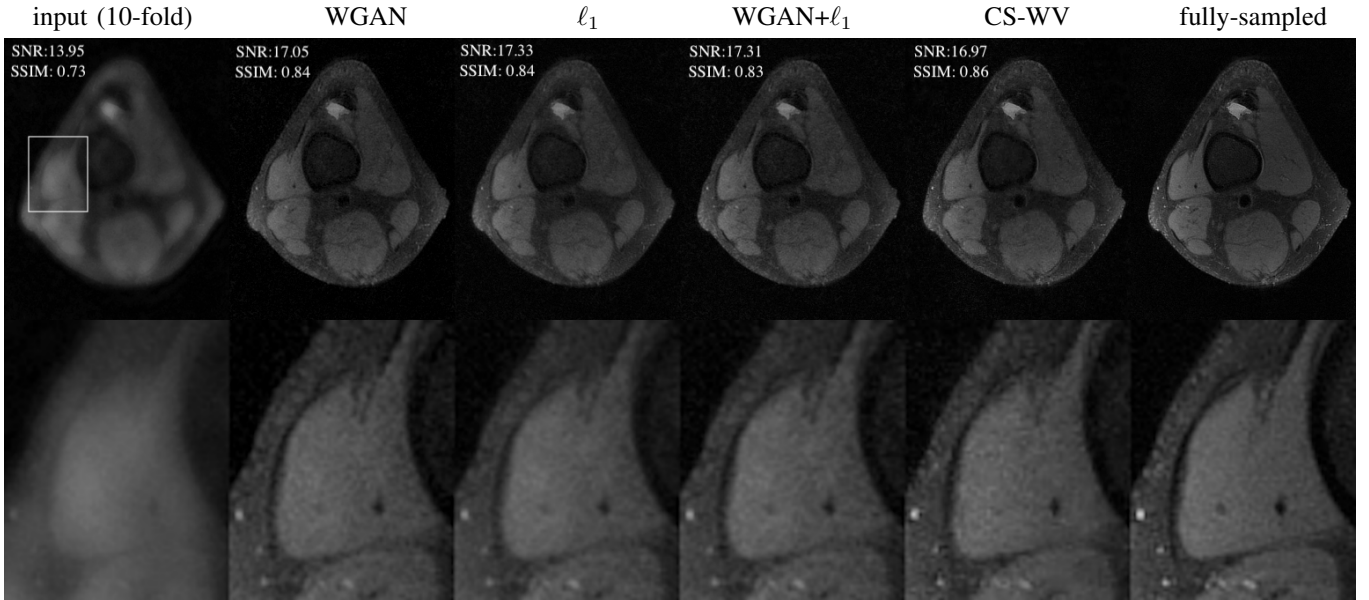


Fig. 12. Test samples from the multi-coil unrolled model trained with various objectives compared with CS. From left to right: 10-fold input, outputs from unpaired model trained with WGAN, paired model trained with ℓ_1 , paired model trained with WGAN and ℓ_1 , CS-Wavelet, fully-sampled reference..

TABLE III
INFERENCE TIME OF PLAIN G, UNROLLED G, AND CS.

| Method | plain G | unrolled G | 30-iter CS |
|------------------|---------|------------|------------|
| Second per slice | 0.022 | 0.025 | 0.4 |

VI. CONCLUSIONS

This paper advocates an unpaired deep learning scheme for MRI reconstruction when high-quality training labels are scarce. Leveraging Wasserstein GANs, a generator network based on unrolled ResNets maps linear image estimates to

mimic the image label distribution. The discriminator network then plays the role of a critic that scores the perceptual quality of generator output images. The Wasserstein loss alleviates the need for pairing among the undersampled input and the diagnostic quality labels. It far extends the scope of prior work [18] for imaging scenarios with scarce training labels. Extensive experiments on MRI knee datasets – comparisons with various existing schemes (i.e. plain generator, ℓ_1 , ℓ_1 +LSGAN, and CS), under different configurations (i.e. paired, unpaired, and disjoint) – corroborate the efficacy of WGANs with an unrolled generator in faithful reconstruction of MRIs.

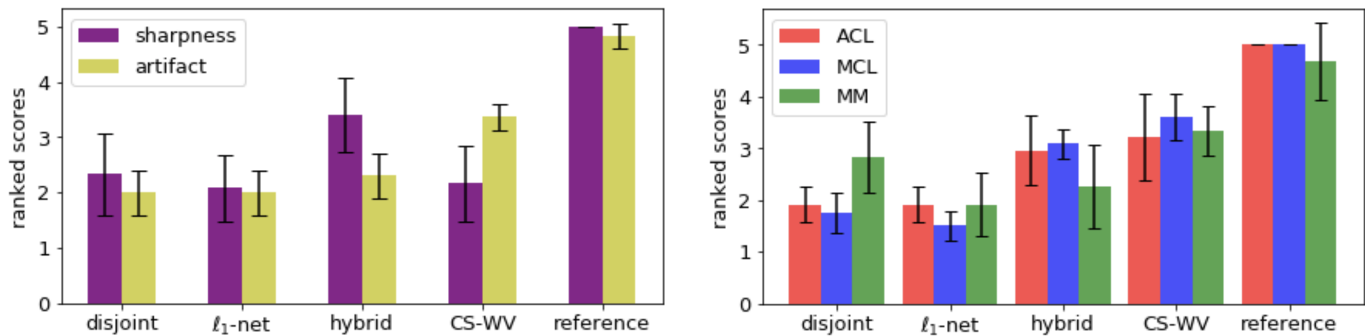


Fig. 13. Ranked score from radiologist review for outputs from disjoint unrolled model, paired unrolled ℓ_1 model, paired unrolled WGAN+ ℓ_1 (hybrid) model, CS-WV, and fully-sampled reference. Aspects of rating: sharpness of the image, level of coherent artifacts, and visibility of three knee structures: ACL, MCL, MM.

There are still important avenues to explore that are on our agenda and part of our ongoing research. One such avenue pertains to training the network with high-quality 2D abdominal images as training labels for reconstructing abdominal cine imaging or DCE imaging frames. Diagnostic quality of recovered images with the expert opinion of radiologists on more test volumes is also an important next step.

REFERENCES

- B. Zhu, J. Z. Liu, B. R. Rosen, and M. S. Rosen, "Image reconstruction by domain transform manifold learning," *Nature*, vol. 555, 03 2018.
- F. Knoll, K. Hammernik, C. Zhang, S. Moeller, T. Pock, D. K. Sodickson, and M. Akcakaya, "Deep Learning Methods for Parallel Magnetic Resonance Image Reconstruction," *arXiv e-prints*, p. arXiv:1904.01112, Apr 2019.
- F. Chen, J. Y. Cheng, V. Taviani, V. R. Sheth, R. L. Brunsing, J. M. Pauly, and S. S. Vasanawala, "Data-driven self-calibration and reconstruction for non-cartesian wave-encoded single-shot fast spin echo using deep learning," *Journal of Magnetic Resonance Imaging*, 2019. [Online]. Available: <https://onlinelibrary.wiley.com/doi/abs/10.1002/jmri.26871>
- C. M. Hyun, H. P. Kim, S. M. Lee, S. Lee, and J. K. Seo, "Deep learning for undersampled MRI reconstruction," *Physics in Medicine & Biology*, vol. 63, no. 13, p. 135007, June 2018. [Online]. Available: <https://doi.org/10.1088/2F1361-6560/2Faac71a>
- J. Y. Cheng, F. Chen, C. Sandino, M. Mardani, J. M. Pauly, and S. S. Vasanawala, "Compressed Sensing: From Research to Clinical Practice with Data-Driven Learning," *arXiv e-prints*, p. arXiv:1903.07824, Mar 2019.
- F. Chen, V. Taviani, I. Malkiel, J. Cheng, J. Tamir, J. Shaikh, S. T. Chang, C. J. Hardy, J. Pauly, and S. S. Vasanawala, "Variable-density single-shot fast spin-echo mri with deep learning reconstruction by using variational networks," *Radiology*, vol. 289, p. 180445, 07 2018.
- J. Y. Cheng, F. Chen, M. T. Alley, J. M. Pauly, and S. S. Vasanawala, "Highly scalable image reconstruction using deep neural networks with bandpass filtering," *CoRR*, vol. abs/1805.03300, 2018. [Online]. Available: <http://arxiv.org/abs/1805.03300>
- C. Qin, J. Schlemper, J. Caballero, A. N. Price, J. V. Hajnal, and D. Rueckert, "Convolutional Recurrent Neural Networks for Dynamic MR Image Reconstruction," *IEEE Transactions on Medical Imaging*, vol. 38, pp. 280–290, 2017.
- J. Schlemper, J. Caballero, J. V. Hajnal, A. N. Price, and D. Rueckert, "A Deep Cascade of Convolutional Neural Networks for Dynamic MR Image Reconstruction," *IEEE Transactions on Medical Imaging*, vol. 37, no. 2, pp. 491–503, Feb 2018.
- K. C. Tezcan, C. F. Baumgartner, and E. Konukoglu, "MR image reconstruction using the learned data distribution as prior," *CoRR*, vol. abs/1711.11386, 2017. [Online]. Available: <http://arxiv.org/abs/1711.11386>
- J. Tamir, S. Yu, and M. Lustig, "Unsupervised deep basis pursuit: Learning reconstruction without ground-truth data," in *Proceedings of the 27th Annual Meeting of ISMRM*, 2019.
- F. Ong and M. Lustig, "k-space aware convolutional sparse coding: Learning from undersampled k-space datasets for reconstruction," in *Proceedings of the 26th Annual Meeting of ISMRM*, 2018.
- F. Chen, J. Y. Cheng, J. M. Pauly, and S. S. Vasanawala, "Semi-Supervised Learning for Reconstructing Under-Sampled MR Scans," in *Proceedings of the 27th Annual Meeting of ISMRM*, 2019.
- K. H. Jin, M. Unser, and K. M. Yi, "Self-supervised deep active accelerated MRI," *CoRR*, vol. abs/1901.04547, 2019. [Online]. Available: <http://arxiv.org/abs/1901.04547>
- S. U. H. Dar and T. Çukur, "A transfer-learning approach for accelerated MRI using deep neural networks," *CoRR*, vol. abs/1710.02615, 2017. [Online]. Available: <http://arxiv.org/abs/1710.02615>
- I. Sánchez and V. Vilaplana, "Brain MRI super-resolution using 3D generative adversarial networks," *CoRR*, vol. abs/1812.11440, 2018. [Online]. Available: <http://arxiv.org/abs/1812.11440>
- G. Yang, S. Yu, H. Dong, G. G. Slabaugh, P. L. Dragotti, X. Ye, F. Liu, S. R. Arridge, J. Keegan, Y. Guo, and D. N. Firmin, "Dagan: Deep de-aliasing generative adversarial networks for fast compressed sensing MRI reconstruction," *IEEE Transactions on Medical Imaging*, vol. 37, pp. 1310–1321, 2018.
- M. Mardani, E. Gong, J. Y. Cheng, S. S. Vasanawala, G. Zaharchuk, L. Xing, and J. M. Pauly, "Deep generative adversarial neural networks for compressive sensing (GANCS) MRI," *IEEE Transactions on Medical Imaging*, vol. 38, no. 1, pp. 167–179, July 2018.
- T. M. Quan, T. Nguyen-Duc, and W.-K. Jeong, "Compressed sensing MRI reconstruction using a generative adversarial network with a cyclic loss," *IEEE Transactions on medical imaging*, vol. 37, no. 6, pp. 1488–1497, 2018.
- Z. Li, T. Zhang, and D. Zhang, "SEGAN: structure-enhanced generative adversarial network for compressed sensing MRI reconstruction," *CoRR*, vol. abs/1902.06455, 2019. [Online]. Available: <http://arxiv.org/abs/1902.06455>
- C. Ledig, L. Theis, F. Huszar, J. Caballero, A. Cunningham, A. Acosta, A. Aitken, A. Tejani, J. Totz, Z. Wang, and W. Shi, "Photo-realistic single image super-resolution using a generative adversarial network," in *2017 IEEE Conference on Computer Vision and Pattern Recognition (CVPR)*, July 2017, pp. 105–114.
- M. Arjovsky, S. Chintala, and L. Bottou, "Wasserstein generative adversarial networks," in *Proceedings of the 34th International Conference on Machine Learning*, ser. Proceedings of Machine Learning Research, vol. 70, 06–11 Aug 2017, pp. 214–223. [Online]. Available: <http://proceedings.mlr.press/v70/arjovsky17a.html>
- K. He, X. Zhang, S. Ren, and J. Sun, "Deep residual learning for image recognition," in *2016 IEEE Conference on Computer Vision and Pattern Recognition (CVPR)*, June 2016, pp. 770–778.
- C. Villani, *The Wasserstein distances*. Berlin, Heidelberg: Springer Berlin Heidelberg, 2009, pp. 93–111. [Online]. Available: https://doi.org/10.1007/978-3-540-71050-9_6
- I. Goodfellow, J. Pouget-Abadie, M. Mirza, B. Xu, D. Warde-Farley, S. Ozair, A. Courville, and Y. Bengio, "Generative adversarial nets," in *Advances in neural information processing systems*, 2014, pp. 2672–2680.
- X. Mao, Q. Li, H. Xie, R. Y. Lau, Z. Wang, and S. P. Smolley, "Least squares generative adversarial networks," in *Computer Vision (ICCV), 2017 IEEE International Conference on*. IEEE, 2017, pp. 2813–2821.

- [27] I. Gulrajani, F. Ahmed, M. Arjovsky, V. Dumoulin, and A. C. Courville, "Improved training of wasserstein GANs," in *Advances in Neural Information Processing Systems*, 2017, pp. 5769–5779.
- [28] C. K. Sønderby, J. Caballero, L. Theis, W. Shi, and F. Huszár, "Amortised MAP inference for image super-resolution," *CoRR*, vol. abs/1610.04490, 2016. [Online]. Available: <http://arxiv.org/abs/1610.04490>
- [29] M. Uecker, P. Lai, M. J. Murphy, P. Virtue, M. Elad, J. M. Pauly, S. S. Vasanawala, and M. Lustig, "Espiritan eigenvalue approach to autocalibrating parallel mri: Where sense meets grappa," *Magnetic Resonance in Medicine*, vol. 71, no. 3, pp. 990–1001, 2014. [Online]. Available: <https://onlinelibrary.wiley.com/doi/abs/10.1002/mrm.24751>
- [30] M. Mardani, Q. Sun, S. Vaswanala, V. Pappas, H. Monajemi, J. Pauly, and D. Donoho, "Neural proximal gradient descent for compressive imaging," in *Proceedings of the 32Nd International Conference on Neural Information Processing Systems*, ser. NIPS'18, 2018, pp. 9596–9606. [Online]. Available: <http://dl.acm.org/citation.cfm?id=3327546.3327627>
- [31] H. K. Aggarwal, M. P. Mani, and M. Jacob, "Multi-shot sensitivity-encoded diffusion MRI using model-based deep learning (MODL-MUSSELS)," *CoRR*, vol. abs/1812.08115, 2018. [Online]. Available: <http://arxiv.org/abs/1812.08115>
- [32] Y. Hu, X. Shi, Q. Tian, H. Guo, M. Deng, M. Yu, C. Moran, G. Yang, J. McNab, B. Daniel, and B. Hargreaves, "Reconstruction of multi-shot diffusion-weighted mri using unrolled network with u-nets as priors," in *Proceedings of the 27th Annual Meeting of ISMRM*, 2019.
- [33] M. Lustig and J. Pauly, "Spirit: Iterative self-consistent parallel imaging reconstruction from arbitrary k-space," *Magnetic resonance in medicine: official journal of the Society of Magnetic Resonance in Medicine / Society of Magnetic Resonance in Medicine*, vol. 64, pp. 457–71, 08 2010.
- [34] A. L. Maas, A. Y. Hannun, and A. Y. Ng, "Rectifier nonlinearities improve neural network acoustic models," in *Proc. ICML*, vol. 30, no. 1, 2013, p. 3.
- [35] J.-Y. Zhu, T. Park, P. Isola, and A. A. Efros, "Unpaired image-to-image translation using cycle-consistent adversarial networks," in *Computer Vision (ICCV), 2017 IEEE International Conference on*, 2017.
- [36] L. Yang, D. Zhang, and G. E. Karniadakis, "Physics-Informed Generative Adversarial Networks for Stochastic Differential Equations," *arXiv e-prints*, p. arXiv:1811.02033, Nov 2018.
- [37] A. Flynn, F. Ong, G. Nahum, J. Cheng, M. Lustig, J. Toh, P. Virtue, S. Amin, S. S. Vasanawala, and U. Tariq, "mridata.org," 2018, <http://mridata.org>.
- [38] S. Ioffe and C. Szegedy, "Batch normalization: Accelerating deep network training by reducing internal covariate shift," in *Proceedings of the 32nd International Conference on International Conference on Machine Learning - Volume 37*, ser. ICML'15. JMLR.org, 2015, pp. 448–456. [Online]. Available: <http://dl.acm.org/citation.cfm?id=3045118.3045167>
- [39] Z. Wang, A. C. Bovik, H. R. Sheikh, and E. P. Simoncelli, "Image quality assessment: from error visibility to structural similarity," *IEEE Transactions on Image Processing*, vol. 13, no. 4, pp. 600–612, April 2004.
- [40] M. Uecker, F. Ong, J. Tamir, D. Bahri, P. Virtue, J. Cheng, T. Zhang, and M. Lustig, "Berkeley advanced reconstruction toolbox," in *Proceedings of the 23rd Annual Meeting of ISMRM*, 2015.
- [41] Nimble Co LLC d/b/a Purview, "Horos." [Online]. Available: <https://horosproject.org>
- [42] NVIDIA. (2019) Titan xp graphics card with pascal architecture. [Online]. Available: <https://www.nvidia.com/en-us/titan/titan-xp/>